Nuclear Materials and Energy 24 (2020) 100766

Contents lists available at ScienceDirect

Nuclear Materials and Energy

journal homepage: www.elsevier.com/locate/nme

Elucidating the microstructure of tungsten composite materials produced by powder injection molding

Michael Duerrschnabel, Steffen Antusch, Birger Holtermann, Ute Jaentsch, Siegfried Baumgaertner, Carsten Bonnekoh, Mirjam Hoffmann, Jan Hoffmann, Michael Rieth

Karlsruhe Institute of Technology (KIT), Institute for Applied Materials, D-76344 Eggenstein-Leopoldshafen, Germany

ARTICLE INFO

Keywords:
Powder injection molding (PIM)
Tungsten
Doped tungsten materials
Scanning electron microscopy (SEM)
Analytical transmission electron microscopy (ATEM)
Mechanical properties

ABSTRACT

A detailed microstructural analysis is one key factor for establishing structure–property relationships, which themselves are essential for manufacturing any device or part thereof. In particular, this paper focuses on the microstructural analysis of tungsten composite materials produced by powder injection molding (PIM). Our combined scanning electron microscopy (SEM) and transmission electron microscopy (TEM) approach revealed that W/TiC and W/Y_2O_3 composites are promising candidates for e.g. plasma facing components in future fusion reactors. The grains size distribution of all present phases was a log-normal one. TiC and Y_2O_3 precipitates in contrast to HfC ones limited the grain growth of the tungsten matrix during sintering about three times more efficient. The precipitate grain size was for all samples in the range of 1.7 µm–3.5 µm. Chemical interaction was only observed for TiC-based composites in the form of W diffusion into the TiC precipitate forming a mixed (Ti, W) carbide retaining the face-centered cubic (fcc) based crystal structure of pure TiC. The tungsten content in Y_2O_3 and HfC precipitates was found to be negligible. La_2O_3 was only observed in TEM attached to (Ti, W)C particles in the form of about 100 nm sized precipitates. As result, the Y_2O_3 and TiC containing samples are considered as promising materials for further detailed mechanical and microstructural investigations.

1. Introduction

Tungsten-based materials are considered as potential plasma-facing materials in future fusion reactors beyond the international nuclear experimental reactor (ITER), since these materials – as is well known by now - exhibit excellent high temperature properties. Among others, typical examples are the exceptional high melting point, a good sputter resistance, a high thermal conductivity, a low thermal expansion, or the remarkable high-temperature (creep) strength [1–4]. Nonetheless, tungsten materials show drawbacks like an extreme brittleness at low temperatures [5,6], which is even more enhanced by neutron irradiation, softening due to recrystallization (the recrystallization temperature can be lower than 1000 °C depending on the degree of deformation) as well as time and cost aspects that come into play in connection with industrial scale fabrication of the reactor components [3,7]. An effective method to resolve these limitations is to manufacture composite materials consisting of a matrix with finely dispersed grains of carbides (e.g. TiC or HfC) and oxides (e.g. Y_2O_3 or La_2O_3) [8–13]. On the one hand, these oxides and carbides are promising, since they have high melting points (e.g. 2410 °C, 2217 °C, 3140 °C, 3890 °C for Y_2O_3, La_2O_3, TiC and HfC, respectively) and on the other hand they should not produce any highly activating isotopes upon neutron irradiation. It is also known that the addition of oxide and carbide particles into a tungsten matrix influences the mechanical behavior of the material like e.g. ductility or strength [1,14–16], which could be further improved by the addition of Rhenium forming a solid solution with Tungsten [17,18]. Furthermore, in order to be useful as a plasma facing component in a fusion reactor the addition of such materials should not worsen the thermal fatigue behavior of the component.

Powder injection molding is a promising route towards large scale, high performance, and low cost production of tungsten-based near net parts with complex geometries [19], which might be used not only as fusion reactor material but in any suitable high temperature environment, like for example, in solar power plants [3]. In contrast to many other fabrication methods, by simple adjustment of the particle volume, PIM offers an easy way to tailor material properties over a wide range according to their later field of application.

In the present work we will focus on the microstructural characterization of unirradiated particle reinforced W-PIM materials. The results of the irradiated materials will be reported separately. The present results will be compared to results found in literature and will be the basis for any future work involving W-based PIM materials, e.g.

E-mail address: Michael.duerrschnabel@kit.edu (M. Duerrschnabel).

https://doi.org/10.1016/j.nme.2020.100766
Received 30 March 2020; Received in revised form 9 June 2020; Accepted 18 June 2020
Available online 24 June 2020

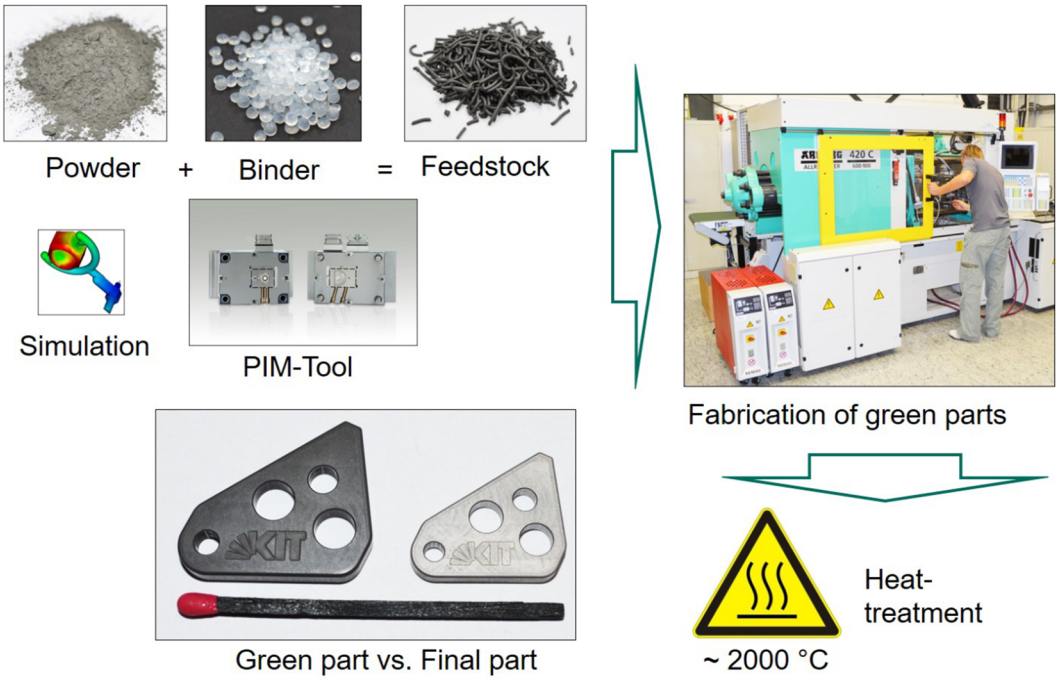

Fig. 1. Schematic illustration of the PIM process.

after neutron irradiation. The characterization of the materials includes a texture analysis via electron backscatter diffraction (EBSD), comprising transmission electron microscopy analyses, and a few basic results from four-point bending tests.

2. Experimental

Several W-PIM small scale specimens (8 mm × 8 mm × 4 mm) of different alloys were produced: W-1TiC, W-1HfC, W-3Re-TiC, W-3Re-2Y_2O_3, and W-1La_2O_3-1TiC- that were tested for high heat flux properties at Forschungszentrum Juelich with parameters as listed in [4,20]. Additional plasma exposure tests have been performed to some of these materials in the Magnum-PSI facility (DIFFER, The Netherlands) [21]. The PIM synthesis (see Fig. 1) of our samples followed the procedure as described by Antusch et al. [1,3,19,22,23]. The five samples mentioned above were analyzed in detail by scanning (SEM) and transmission electron microscopy as well as by mechanical testing, i.e. 4-point-bending tests. Prior to microstructural analyses the sample surfaces have been prepared by an optimized procedure that included grinding, polishing and subsequent electropolishing to balance surface topography and surface damage.

The 4-point bending tests were carried out in a Zwick 100 testing machine under vacuum conditions with the testing temperature ranging from 200 °C to 800 °C using test geometries according to [24,25]. The loading rate in all tests was 0.033 mm/min. Basic tensile properties have been partly determined and published in [26].

The SEM analyses namely Electron backscatter diffraction and energy-dispersive X-ray analysis (EDX) were carried out in a Zeiss Merlin and a Zeiss Auriga with high tensions ranging from 5 kV to 20 kV. The textural analysis of the present W-based composite materials was performed by using a Zeiss Merlin field-emission-gun scanning electron microscope equipped with an EDAX Hikari high-speed EBSD camera. The SEM acceleration voltage was set to 20 kV with a probe current of 10nA. The SEM-EDX analysis was carried out using two machines: (i) Zeiss Merlin and (ii) Auriga CrossBeam focused ion beam/scanning electron microscope (FIB/SEM). In the Merlin machine we used the same acceleration voltage and probe currents as in the EBSD measurements. The Zeiss Auriga was used for two purposes: (i) EDX mapping of light elements at lower acceleration voltage and preparation of a lamella for TEM.

Transmission electron microscopy (TEM) characterization was performed in a Thermofisher Talos F200X scanning transmission electron microscope (STEM) equipped with four EDX detectors and a Gatan Enfinium electron energy-loss (EEL) spectrometer with DualEELS capability. The microscope was operated at 200 kV acceleration voltage. The convergence and the collection angle for the EELS experiments were 10.5 and 14.1 mrad, respectively. The STEM-EDX maps were acquired for than 1 h. The spot size therein did not exceed 1 nm. The EDX detector resolution is specified by the manufacturer as ≤136 eV at Mn-Kα. At the W-Lα (E = 8.396 keV) or Re-Lα (E = 8.651 keV) the energy resolution has a value of about 150–160 eV, which is sufficient to separate both X-ray lines. If the M-Lines of both elements are considered the detector resolution is not sufficient for a clear line separation of both elements. Therefore, the X-ray L-lines are preferred for the EDX analysis if applicable. Quantification of STEM-EDX data was done using the k-factor method, whereas in STEM-EELS Hartree-Slater cross-sections were used in combination with a multiple scattering correction. The TEM images and selected area diffraction pattern (SAED) were acquired by using a Thermofisher Ceta 16 M CCD camera.

3. Results and discussion

3.1. 4-point bending tests

In the following, we defined ductile vs. brittle material behavior as follows: (1) Fracture within the elastic range means brittle behavior, (2) if a fracture appears after plastic deformation but before maximum deflection at 1.5 mm, the behavior is denoted “partially ductile”, and if up to maximum deflection no fracture occurs, we call it “fully ductile” (see Fig. 2).

All samples were analyzed by 4-point bending tests in the range between 200 °C and 800 °C. Table 1 summarizes the maximum flexural strength being obtained. At 200 °C all of the samples were partially ductile or brittle, whereas at 400 °C only W-3Re-2Y_2O_3 and W-3Re-1TiC remained only partially ductile. Above 400 °C W-3Re-2Y_2O_3 was the only partially ductile sample. It exhibited a maximum flexural strength

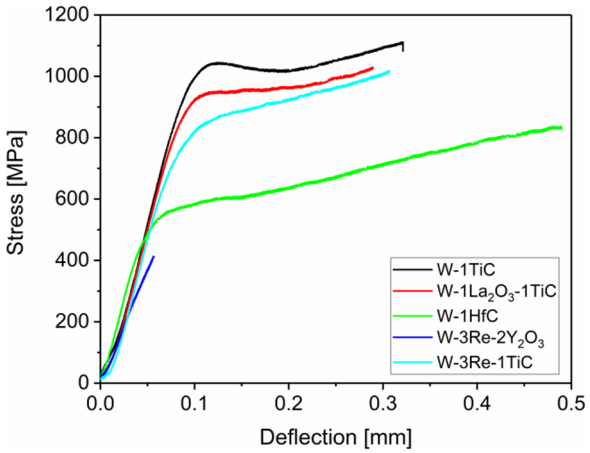

Fig. 2. Stress vs. deflection obtained from 4-point bending tests carried out at 200 °C for all five samples. All materials showed partial ductility with the exception of W-3Re-$2Y_2O_3$, which broke in a brittle manner.

Table 1
Maximum flexural strength in units of MPa and temperature for all analyzed samples. Values marked by a star (*) denote measurements in which the maximum deflection of 1.5 mm was reached.

Sample	200 °C	400 °C	600 °C	800 °C
W-1TiC	1112	1262*	1403*	1277*
W-1La_2O_3-TiC	1030	1493*	1147	501
W-1HfC	837	1030*	–	–
W-3Re-1TiC	413	1446	911	976
W-3Re-$2Y_2O_3$	1018	1572*	1743*	1564

of 1493 MPa at 400 °C and for all other measured temperatures it was below this value. A similar behavior with a maximum yield strength at 400 °C was also observed by Aguirre et al. [2] for a W/Y_2O_3 composite material suggesting that our observed trend in flexural strength for sample W-3Re-$2Y_2O_3$ might be a characteristic feature of this material. The carbide containing samples in general yielded a higher flexural strength than W-3Re-$2Y_2O_3$.

3.2. Texture analysis by SEM-EBSD

Fig. 3 shows EBSD orientation mappings for all analyzed samples for two different length scales. The EBSD mappings reveal an isotropic microstructure, i.e. equiaxed grain orientations, which has already been found by Antusch et al. in similar processed materials [1,23]. This is a clear benefit of the PIM method. The lower magnification orientation maps were further evaluated with respect to W matrix grain sizes in order to have good statistics. The higher magnified insets show that the EBSD indexation procedure fails for the secondary phase precipitates (black & white color). Due to the sample preparation method a residual topography was left on the sample hampering the EBSD analysis of oxide and carbide precipitates. The precipitates' structure and composition will be addressed separately in detail in the following sections. The grain size distribution as well as the average grain size are plotted for all five samples in the down most row of Fig. 3. The W matrix grain size distributions follow a log-normal type for all samples as expected. However, there are distinct differences between the single samples that have to be addressed. The distribution width increases in the following order, which is also reflected by the average grain size: W-3Re-$2Y_2O_3$, W-1La_2O_3-1TiC, W-1TiC, W-3Re-1TiC, W-1HfC. Sample W-3Re-TiC additionally showed a bimodal matrix grain size distribution, which is most probably due to a problem during the powder mixing procedure. In terms of W grain boundary pinning, i.e. recrystallization inhibition, Y_2O_3 is the most effective material, whereas HfC performs poorest given the actual synthesis conditions. The W grain size is an important quantity, because it influences for example hardness, strength, fatigue and toughness in general, but also high heat flux test properties like surface roughening and crack formation [4], which are important for the thermo-mechanical behavior of the material. The later plays amongst others an important role for the qualification as a divertor armor material in a future fusion reactor.

3.3. Secondary phases analysis by SEM

Fig. 4 shows Z contrast images (i.e. BSE images) and EDX elemental maps on the micrometer scale for 4 of the 5 samples. Sample W-1La_2O_3-TiC was emitted since the results were similar to W-1TiC except for the grain size as can be seen in Table 2. Grain sizes were determined from a larger region than presented in Fig. 4 including several hundred precipitates for statistical reasons. The EDX mappings reveal that the matrix materials (W or W/Re) infiltrate larger TiC precipitates, whereas smaller ones seem to be less affected. In sample W-1HfC the Hf and W maps show a similar behavior, which can be hardly seen, since the infiltration process of matrix elements into the HfC precipitates is almost completed, i.e. precipitates and matrix intermix. This particular effect has already been observed in literature for W/ZrC composite materials [27,28], but also for W/TiC [29] and affects in principle every W/carbide system, as Holleck summarized already roughly 40 years ago [30]. He found a complete miscibility of several transition metal carbide combinations for temperatures in the range between 2000 °C and 3000 °C. Sintering temperatures, which also need to be applied to PIM samples, often lie within or near that range and, hence, we expect to observe mixed carbides. From a thermodynamic point of view, it can be explained by examining the Gibbs free energies of formation and the ionic radii. For example, in case of the W-TiC system Song et al. [29] explained the existence of a mixed carbide by (i) the similar ionic radii of Ti and W (74 pm and 66 pm [31]) facilitating solid state interdiffusion of Ti and W atoms and (ii) the lower free energy of formation of TiC compared to WC or W_2C, which suggests that free carbon gets bound in the Ti/W mixed carbide instead of forming separate WC or W_2C precipitates.

The oxide containing material, i.e. W-3Re-$2Y_2O_3$ behaves quite different compared to the carbide materials. The EDX mappings presented in Fig. 4 (rightmost column) show that the yttrium oxide precipitates are smaller compared to the carbide samples (see also Table 2) and that there is no significant diffusion of matrix elements into the precipitate being observed. This might be explained by (i) the greater ionic radius difference of Y and W (90 pm and 60 pm) hampering solid state diffusion and (ii) the large difference in free energy of formation between Y_2O_3 and WO_2 or WO_3 (which is roughly about 700 kJ/mol up to 1500 K [32]). In addition, Lassner and Schubert neither mention any intermetallic compound of rare-earth and tungsten nor anything about a reaction of tungsten with Y_2O_3 [33]. So far, only tungsten oxide seems to react above 1000 °C with Y_2O_3 forming yttrium tungstate as reported by Borchardt [34]. For Re ions a similar argumentation should be valid. However, due to the larger initial concentration of Y_2O_3 in the raw material, the number density of Y_2O_3 precipitates is high. This still needs to be optimized with respect to material properties vs. materials costs.

3.4. Secondary phase analysis by TEM

The STEM-EDX measurements presented in Fig. 5 show that the matrix in sample W-1TiC consists of W, whereas as the precipitate consists of Ti and C. However, the W intensity inside the precipitate is not zero. Furthermore, one can see the limitations of the PIM technique: on the right side above the TiC particle a small La oxide particle is located, which presumably is a residue from an earlier processed sample batch. We tried a quantitative evaluation of the STEM-EDX data (see Table 3) for all observed phases, However, due to the sample

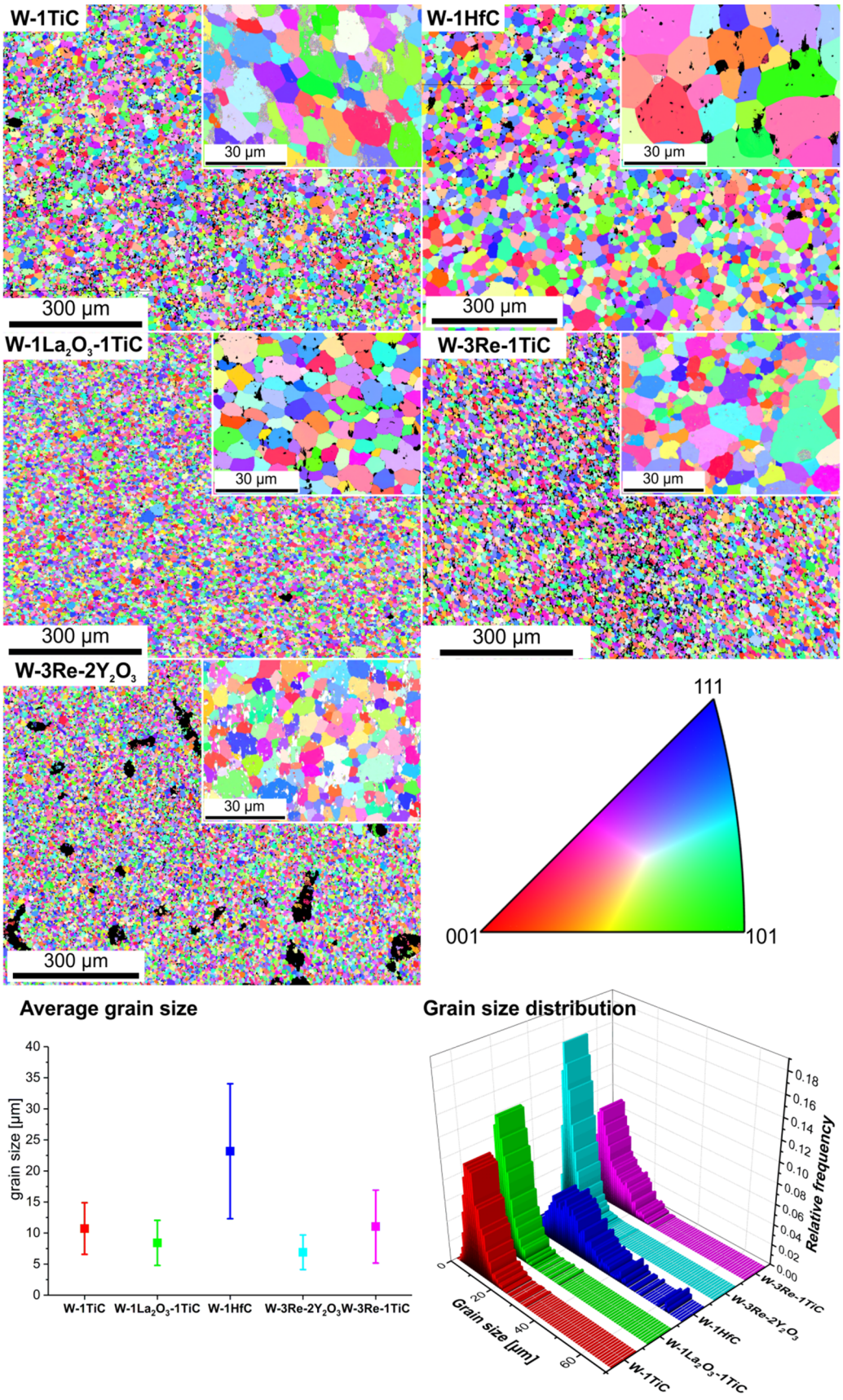

Fig. 3. EBSD mappings revealing the texture of the W matrix for all analyzed materials. The large-scale mappings were used to determine the grain size distribution and an average grain size for the matrix. The insets show magnified regions to illustrate that the indexing fails (black or noisy regions) for secondary phase regions.

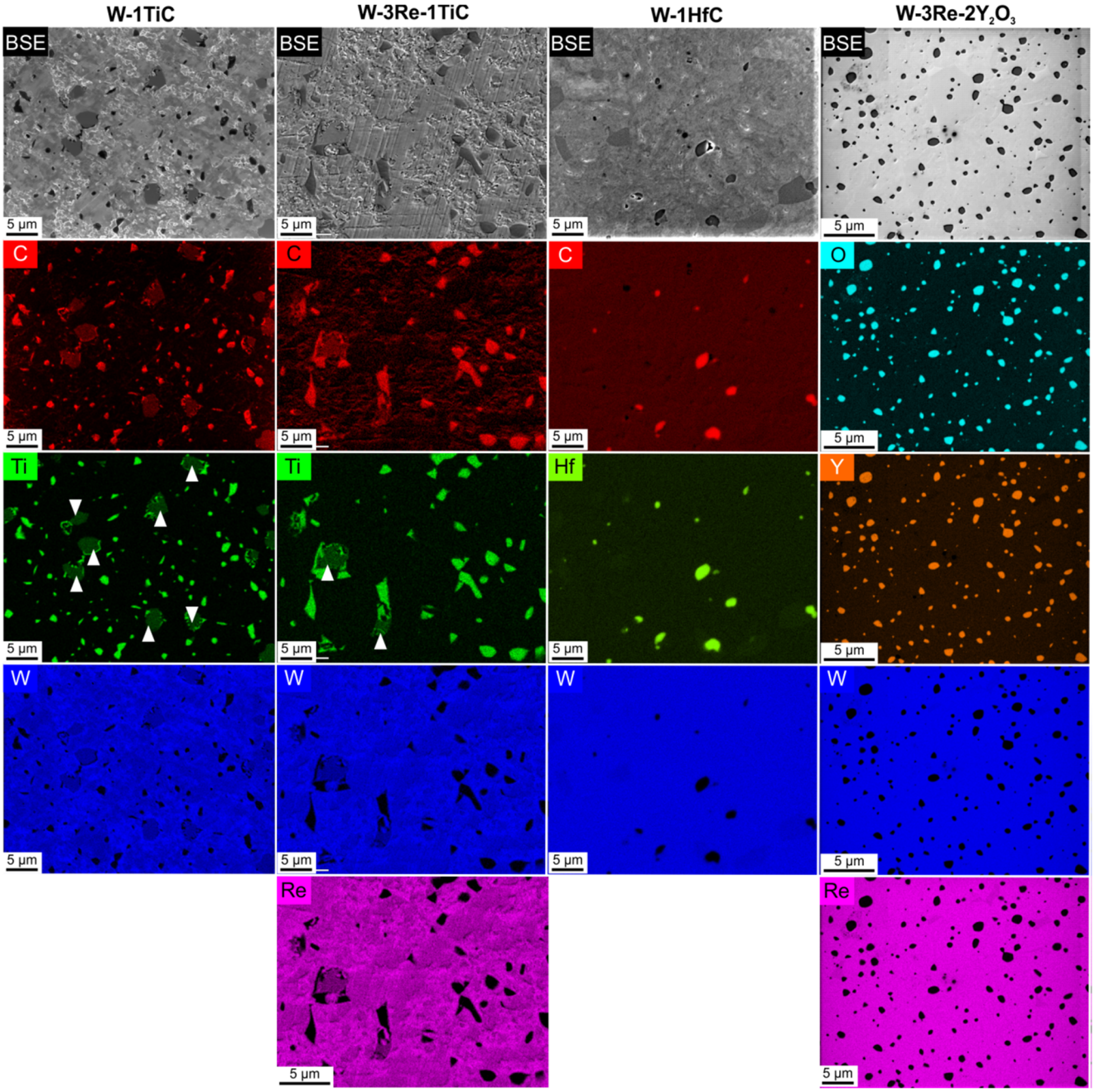

Fig. 4. Backscatter electron images (BSE) and EDX elemental mappings of four samples. Sample W-1TiC-1La_2O_3 was excluded because it looked similar to W-1TiC and W-3Re-1TiC. The white triangles within the Ti map indicate some grains, where W infiltration was observed.

Table 2
Average grain size of precipitates determined by EDX in the SEM. The statistics includes more than 100 precipitates per sample.

Sample	Volume percent carbide or oxide	Average precipitate grain size [µm]
W-1TiC	3.80	3.51 ± 2.20
W-1La_2O_3-TiC	3.73	1.69 ± 1.12
W-1HfC	1.57	3.30 ± 3.46
W-3Re-1TiC	4.08	2.27 ± 1.86
W-3Re-2Y_2O_3	7.31	2.13 ± 1.24

consisting of a heavy element matrix with lighter element inclusions, X-ray absorption is severe problem hampering the exact composition determination of nanometer-sized precipitates. Another obstruction in the EDX analysis of this particular sample was the strong stray radiation from the Mo sample grid as well as from close sample holder parts. Since the carbon distribution in the EDX map is quite noisy, we tried STEM-EELS mapping for a better signal-to-noise ratio as can be seen in the lower part of Fig. 5. W was not be mapped by STEM-EELS, because it is already evident from STEM-EDX that W is contained in the carbide precipitate. In order to further characterize the carbide precipitate STEM-EELS measurements as well as diffraction data was acquired. A quantitative evaluation of a wide-range EELS spectrum taken inside the carbide phase, which is not presented here, results in a C content of about 60 at%. This value 10 at% too high compared to the nominal value, which is most likely due to surface contamination. The Ti and W contents were determined both to be about 20 at%, respectively. However, as shown in Fig. 4 the local Ti and W content might vary from precipitate to precipitate, since Ti and W mix easily at temperatures

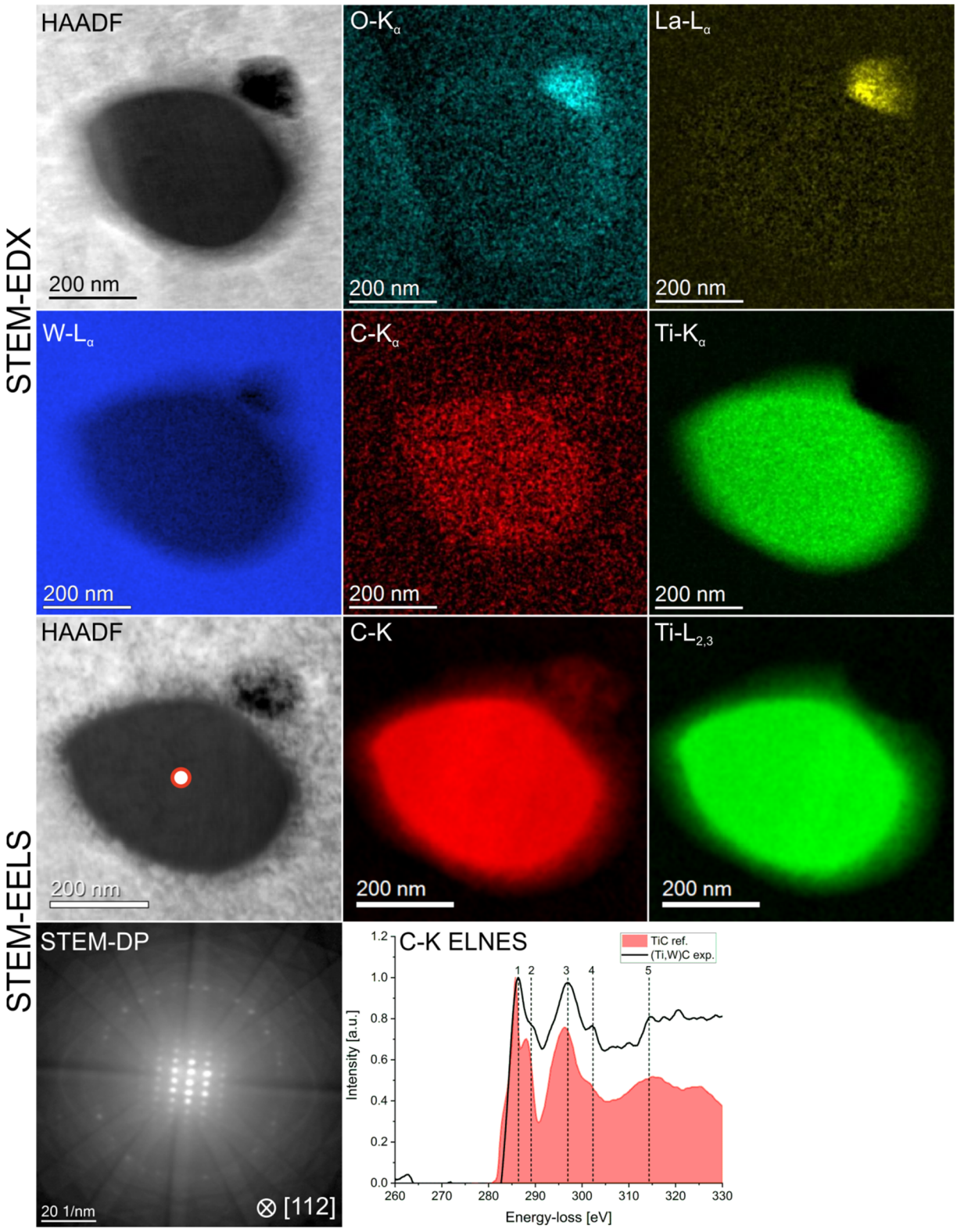

Fig. 5. STEM-EDX elemental mapping (top two rows), STEM-EELS elemental mapping (third row), convergent beam diffraction pattern (acquired from the indicated position in the HAADF image) and measured C-K ELNES compared to a reference [35] (down most row) of sample W-1TiC.

larger than 2000 °C as already discussed above. In Table 3 the oxygen content of the precipitate is overestimated due to a poor fitting in the low energy range during the quantification procedure and is therefore considered at least partially as artifact. Nonetheless, a manual cross-check of the raw EDX spectra showed that a small O peak was present everywhere on the sample corresponding to about 8 at% of O, which is attributed to surface oxidation. Since only a very limited number of small precipitates can be analyzed in TEM, further analysis is required to confirm the data presented in Table 3. Additionally, a STEM diffraction pattern was acquired from the carbide precipitate. A careful

Table 3
Quantification results of EDX data using the k-factor method of STEM-EDX data (including 1-2 precipitates per sample) applying principal component analysis (PCA) and subsequent model fitting implemented in the Hyperspy program package [37].

Sample	Phase	C [at%]	O [at%]	Ti [at%]	La [at%]	Y [at%]	Hf [at%]	W [at%]	Re [at%]
k-factor		1.0000	0.7015	0.3254	1.0161	4.3946	1.2211	1.2776	1.3083
W-1TiC	**W matrix**	5.64	9.15	0.80	1.49	–	–	82.92	–
	(Ti,W) carbide	21.42	27.07	43.53	–	–	–	7.02	–
	La oxide	17.98	50.57	0.00	27.76	–	–	3.69	–
W-1La_2O_3-TiC	**W matrix**	1.64	11.74	0.34	3.43	–	–	82.84	–
	(Ti,W) carbide	54.58	0.00	39.45	0.22	–	–	5.75	–
	La oxide	24.38	19.35	0.00	39.50	–	–	16.77	–
W-1HfC	**W matrix**	7.00	–	–	–	–	2.00	91.00	–
	Hf carbide	37.82	–	–	–	–	55.72	6.46	–
W-3Re-1TiC	**W matrix**	6.72	–	1.77	–	–	–	85.81	5.70
	(Ti,W) carbide	21.65	–	59.06	–	–	–	19.29	0.00
W-3Re-2Y_2O_3	**W matrix**	–	6.35	–	–	1.36	–	86.88	5.41
	Y oxide	–	63.24	–	–	36.05	–	0.47	0.24

evaluation yielded that it corresponds to the [112] zone-axis of TiC (ICSD No. 1546). However, replacing half of the Ti by W only changes the lattice parameter by about 0.008 Å (TiC: ICSD No. 1546, (Ti0.5W0.5)C: ICSD No. 77553), i.e. one cannot distinguish between TiC and (Ti, W)C by electron diffraction. This is also reflected in the C-K ELNES as shown in Fig. 5. Our measurement fits quite well to the reference from Craven and Garvie [35] if the peak positions of both spectra are compared. However, there are differences in their height: peak 1 is the most intense for pure TiC, whereas in (Ti, W)C peak 1 and 3 are equal in height. Peak 2 can be well separated from peak 1 in pure TiC, whereas peak 2 is a shoulder of peak 1 in (Ti, W)C. For peaks 3 and 4 the situation is reversed. Peak 5 in (Ti, W)C is a single peak, whereas in pure TiC it separates into 2 individual peaks. The differences between both spectra we believe to originate from three sources: (i) our energy resolution of 1 eV is about 3 larger that of Craven and Garvie, (ii) the sample thickness of our sample is about 4 times larger than that used by Craven and Garvie due to FIB sample preparation, and (iii) the incorporation of W in the TiC might alter the peak heights present in the C-K ELNES.

Fig. 6a show a dark-field image of a HfC grain. The selected area diffraction pattern shown in Fig. 6b confirms that the grain is still crystalline and fits to the [013] zone-axis of HfC (ICSD No. 159873). The STEM-EDX mapping shown in Fig. 6c and Table 3 confirm that the metal part of the precipitate is Hf with only a small fraction of W. This is in contrast to the TiC containing samples and in agreement with the SEM observations. Despite the higher melting point of HfC compared to TiC (3890 °C vs. 3140 °C), HfC seems to dissolve in the presence of W faster than TiC – only the most stable HfC remain after our sintering procedure.

Fig. 7 shows a combined STEM-EDX/STEM-EELS analysis of a precipitate located at a triple junction in sample W-1TiC-La_2O_3. As already shown in Fig. 5 part of the Ti is replaced by W and a similar argumentation should as above should hold. In addition to that a small (about 100 nm in width) lanthanum oxide particle was found at the lower left edge of the (Ti, W)C particle. By evaluating the STEM-EELS elemental mapping it was possible to quantify the elemental contents of C, O, Ti, and La in units of atoms per nm^3. W was not included, but from the C content an equal concentration to the Ti concentration is derived. In case of the lanthanum oxide the oxygen concentration is too low for La_2O_3. Part of the oxygen in lanthanum oxide might be replaced by carbon.

Fig. 8 combines chemical with structural data of Y_2O_3 precipitates in sample W-3Re-2Y_2O_3. The first row contains STEM-EDX data, i.e. a HAADF image and the elemental mappings of O, Y, W, and Re. Almost no intermixing of matrix elements (W, Re) with the Y_2O_3 precipitates is observed, which is confirmed by the quantitative evaluation presented in Table 3. The residual tungsten concentration in Y_2O_3 might also -at least partly- be due to stray radiation. The Y_2O_3 precipitates are in most cases located at W grain boundaries or triple junctions. However, also Y_2O_3 precipitates inside single W grains were observed, which is believed to be the result of tungsten grain growth during sintering. In order to check the crystallinity of the sample, selected area diffraction pattern as well as atomic resolution STEM images were acquired (left side of second row in Fig. 8). The Y_2O_3 (ICSD No. 23811) precipitate was oriented in [1 1 0] zone-axis. In the magnified region of the STEM image located above the diffraction pattern an atomic model of Y_2O_3 in [1 1 0] orientation was overlaid to assign the atomic columns. Yttrium atoms are depicted in blue and oxygen ones in red. In addition, the ELNES of the O-K edge acquired inside a Y_2O_3 precipitate was monitored and compared to a reference one measured by Zhang et al. [36]. Energy-loss values of the single ELNES peaks in our measurement are comparable to those of the reference; only for peaks 4 to 6 slight differences are observed, which might be due to different acquisition conditions (e.g. sample orientation, energy resolution etc.).

4. Conclusions & outlook

Five tungsten-based composite materials were analyzed by electron microscopy with respect to their microstructure. Preliminary mechanical data, i.e. flexural strength measured by 4-point bending tests, were also recorded. To establish reliable structure–property relationships in these materials, more tests are required, which will be performed later. The tungsten matrix grain size derived from SEM-EBSD measurements follows a log-normal distribution for all samples. The smallest grain size was measured with an average grain size of 5 ± 2 µm in sample W-3Re-2Y_2O_3, whereas the largest matrix grain size was measured with 14 ± 8 µm in sample W-1HfC, i.e. Y_2O_3 precipitates are the best performing grain stabilizers (tungsten grain growth suppression) within this study for the sintering process. For sample W-3Re-TiC a bimodal matrix grain size distribution was observed, which was most probably due to a problem during the powder mixing procedure. SEM-EDX revealed that the tungsten matrix and TiC easily mix at temperatures of 2000 °C and beyond, and that the process seems to be faster for HfC. TEM measurements revealed the formation of a (Ti, W) mixed carbide, in Hf containing samples the effect was negligible. The crystal structure of the (Ti, W) mixed carbide precipitates was still fcc like in pure titanium carbide and did not change into a hexagonal one as expected from pure tungsten carbides. The least interaction with the tungsten matrix was observed for Y_2O_3 precipitates, which were not noticeably modified in structure or composition under the used sintering conditions as proven by selected area diffraction, atomic resolution STEM imaging and ELNES measurements. La_2O_3 was only observed in TEM attached to (Ti, W)C particles in the form of about 100 nm sized precipitates. All by TEM measured precipitates were still crystalline and were preferentially located at grain boundaries or triple junctions. In summary, the Y_2O_3 and TiC containing samples are promising for further mechanical and microstructural investigations.

The future course of action for the further analysis of tungsten-based

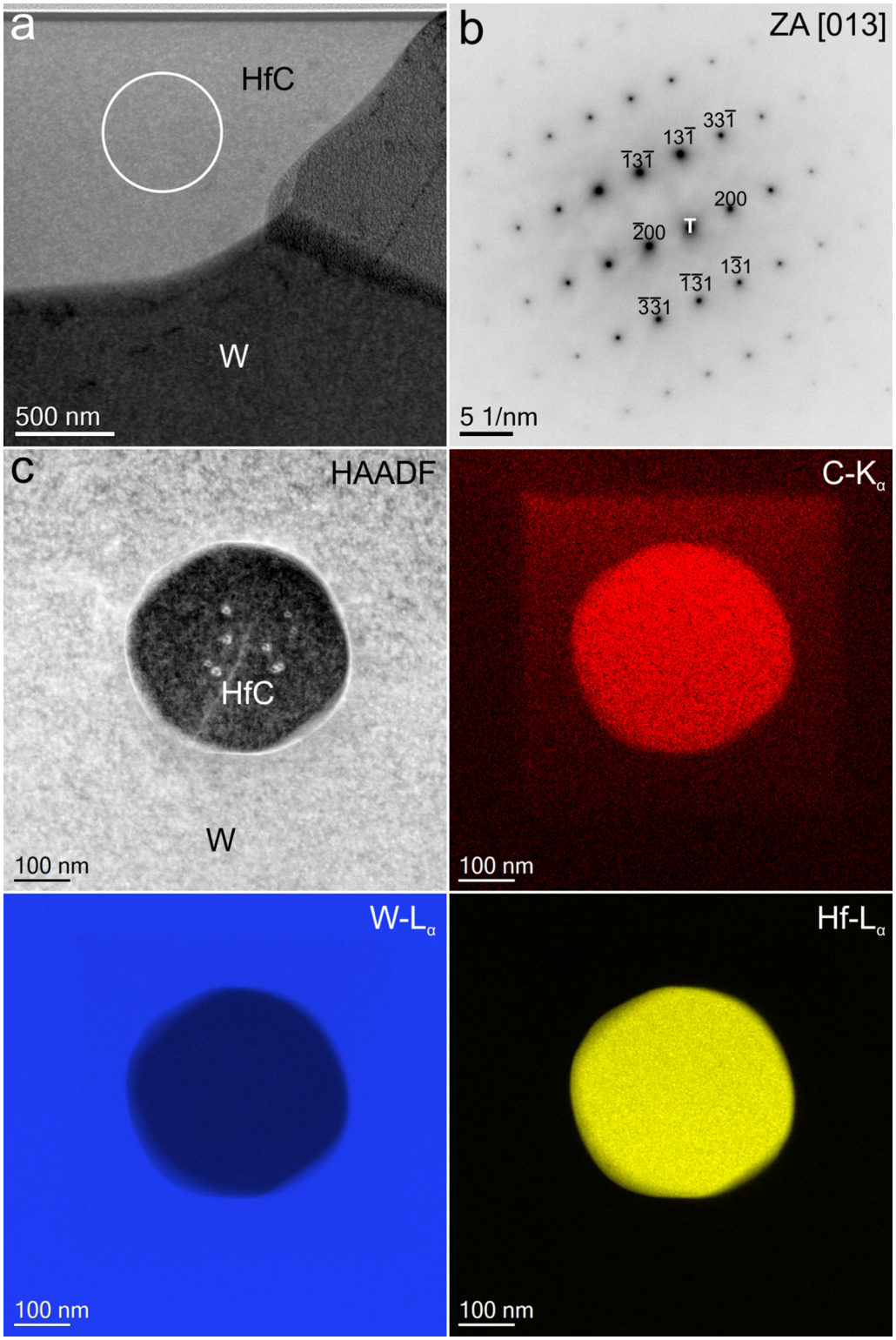

Fig. 6. (a) Dark-field image of a HfC grain and (b) corresponding selected area diffraction pattern in [013] zone-axis orientation. (c) HAADF image and STEM-EDX mapping of a smaller, spherical shaped HfC grain. The additional intensity in the C map is due to surface contamination during the measurement.

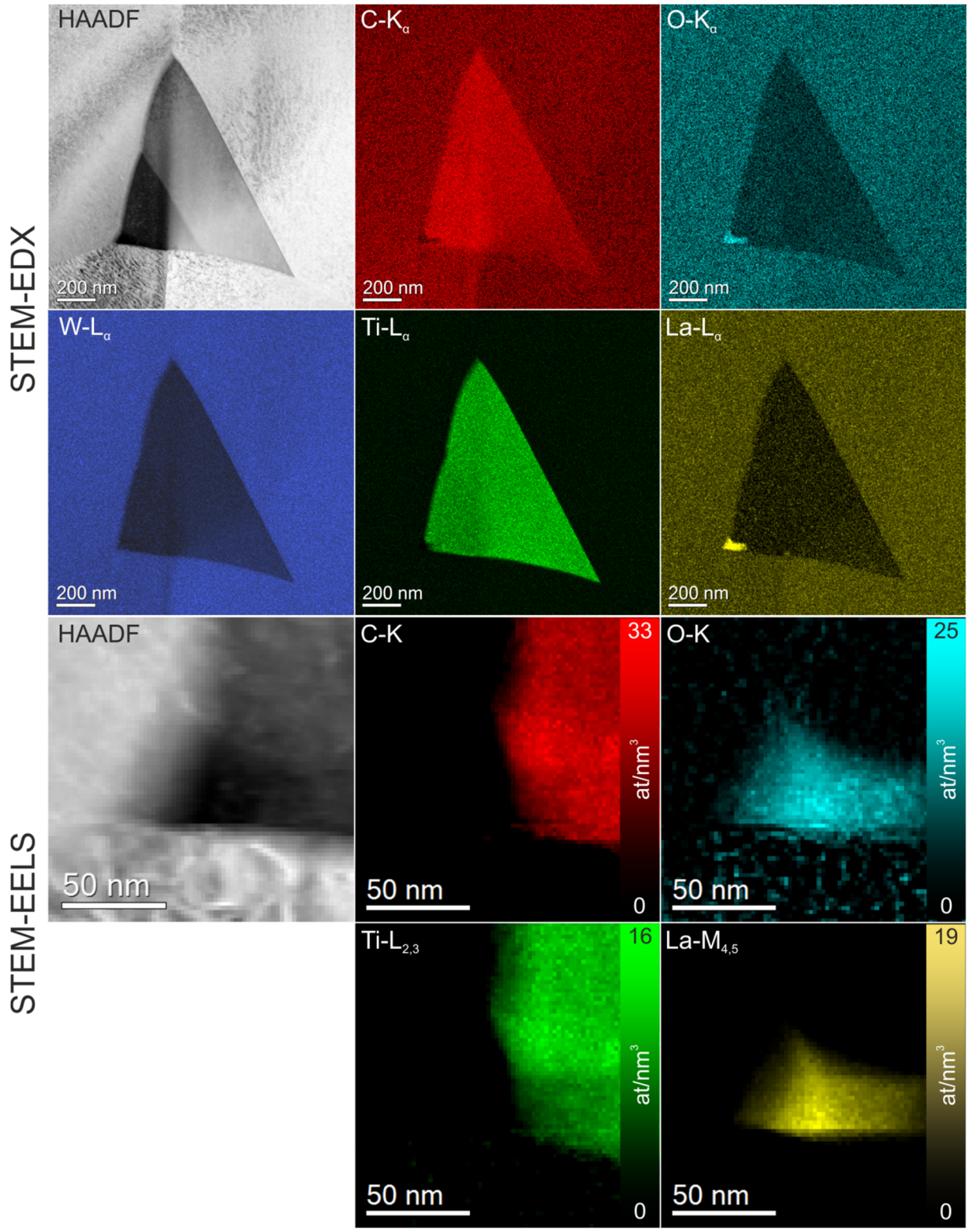

Fig. 7. STEM-EDX and STEM-EELS elemental mapping of a (Ti, W)C precipitate in sample W-1TiC-La_2O_3. The STEM-EELS maps show a magnified area located at the lower left corner of the precipitate in which remains of La_2O_3 are located.

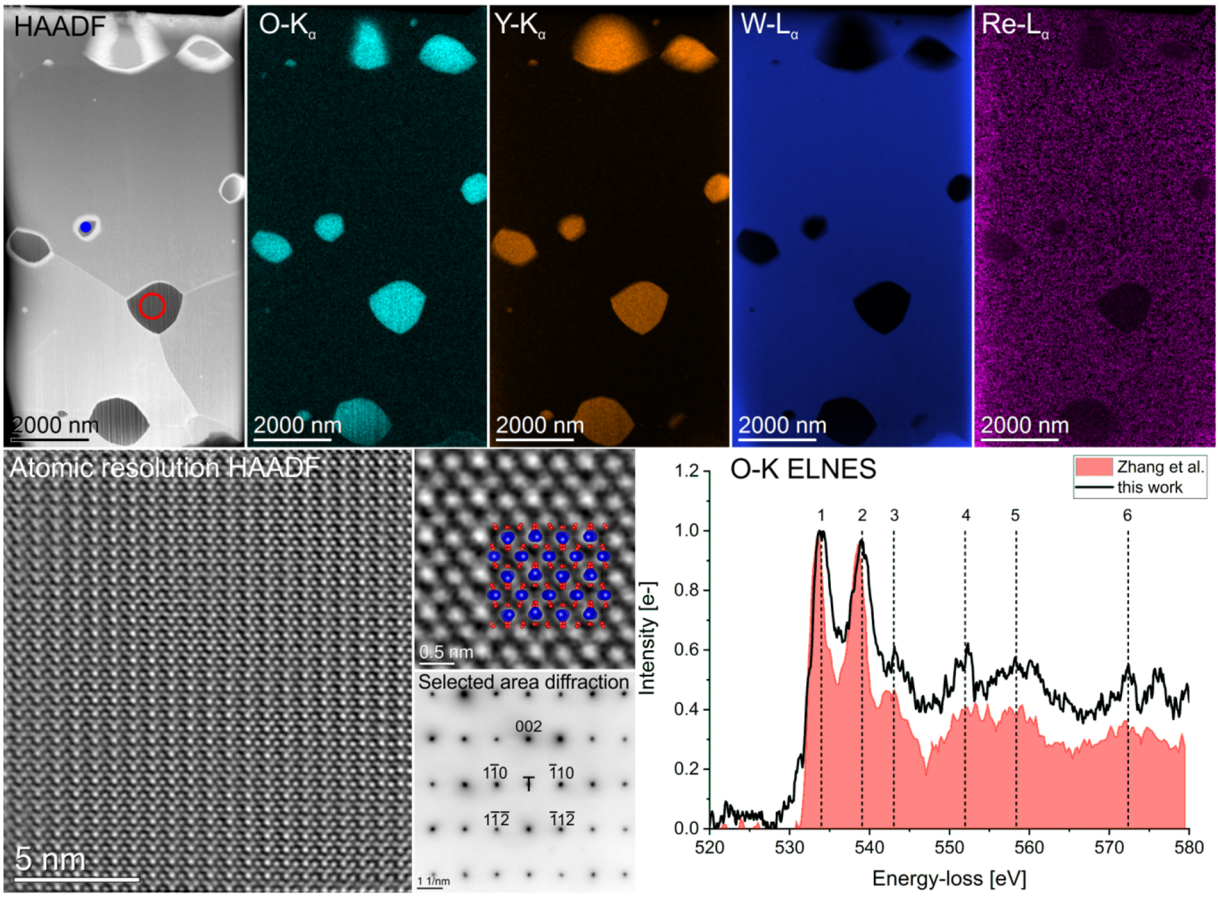

Fig. 8. The first row of images shows the results of a STEM-EDX elemental mapping. The second row shows an atomic resolution STEM-HAADF image of a Y_2O_3 particle oriented in [110] zone-axis and the measured ELNES of the O-K edge compared to a reference [36]. The upper small image in the center shows an enlarged region of the HRSTEM image overlaid by an atomic model (blue: Y, red: O) and the lower image shows a SAED pattern.

composite materials will include more and different material tests, improved sample preparation (minimized surface topography) by the use of an ion cross section mill, a variation of the Y_2O_3 content to find an optimum, and finally a comparison with the irradiated samples to assess their potential use as an plasma facing material in DEMO under operating conditions.

CRediT authorship contribution statement

Michael Duerrschnabel: Writing - original draft, Investigation, Visualization, Writing - review & editing. **Steffen Antusch:** Project administration, Supervision, Writing - review & editing, Conceptualization. **Birger Holtermann:** Investigation. **Ute Jaentsch:** Investigation. **Siegfried Baumgaertner:** Investigation. **C. Bonnekoh:** Investigation. **Mirjam Hoffmann:** Investigation. **Jan Hoffmann:** . **Michael Rieth:** Funding acquisition, Project administration, Supervision, Writing - review & editing, Conceptualization.

Declaration of Competing Interest

The authors declare that they have no known competing financial interests or personal relationships that could have appeared to influence the work reported in this paper.

Acknowledgement

This work has been carried out within the framework of the EUROfusion Consortium and has received funding from the Euratom research and training programme 2014-2018 and 2019-2020 under grant agreement No 633053. The views and opinions expressed herein do not necessarily reflect those of the European Commission.

References

[1] S. Antusch, J. Hoffmann, A. Klein, J.P. Gunn, M. Rieth, T. Weingaertner, Processing of complex near-net-shaped tungsten parts by PIM, Nucl. Mater. Energy. 16 (2018) 71–75, https://doi.org/10.1016/j.nme.2018.05.023.

[2] M.V. Aguirre, A. Martín, J.Y. Pastor, J. Llorca, M.A. Monge, R. Pareja, Mechanical behavior of W-Y2O3 and W-Ti Alloys from 25 °C to 1000 °C, Metall. Mater. Trans. A Phys. Metall. Mater. Sci. 40 (2009) 2283–2290, https://doi.org/10.1007/s11661-009-9956-4.

[3] S. Antusch, J. Reiser, J. Hoffmann, A. Onea, Refractory Materials for Energy Applications, Energy Technol. 5 (2017) 1064–1070, https://doi.org/10.1002/ente.201600571.

[4] G. Pintsuk, S. Antusch, M. Rieth, M. Wirtz, Manufacturing and characterization of PIM-W materials as plasma facing materials, Phys. Scr. 2016 (2016) 1–6, https://doi.org/10.1088/0031-8949/T167/1/014056.

[5] S. Nogami, S. Watanabe, J. Reiser, M. Rieth, S. Sickinger, A. Hasegawa, A review of impact properties of tungsten materials, Fusion Eng. Des. 135 (2018) 196–203, https://doi.org/10.1016/j.fusengdes.2018.08.001.

[6] M. Rieth, A. Hoffmann, Int. Journal of Refractory Metals and Hard Materials Influence of microstructure and notch fabrication on impact bending properties of tungsten materials, RMHM. 28 (2010) 679–686, https://doi.org/10.1016/j.ijrmhm.2010.04.010.

[7] M. Rieth, S.L. Dudarev, S.M. Gonzalez De Vicente, J. Aktaa, T. Ahlgren, S. Antusch, D.E.J. Armstrong, M. Balden, N. Baluc, M.F. Barthe, W.W. Basuki, M. Battabyal, C.S. Becquart, D. Blagoeva, H. Boldyryeva, J. Brinkmann, M. Celino, L. Ciupinski, J.B. Correia, A. De Backer, C. Domain, E. Gaganidze, C. García-Rosales, J. Gibson, M.R. Gilbert, S. Giusepponi, B. Gludovatz, H. Greuner, K. Heinola, T. Höschen, A. Hoffmann, N. Holstein, F. Koch, W. Krauss, H. Li, S. Lindig, J. Linke, C. Linsmeier, P. López-Ruiz, H. Maier, J. Matejicek, T.P. Mishra, M. Muhammed, A. Muñoz, M. Muzyk, K. Nordlund, D. Nguyen-Manh, J. Opschoor, N. Ordás, T. Palacios, G. Pintsuk, R. Pippan, J. Reiser, J. Riesch, S.G. Roberts, L. Romaner, M. Rosiński, M. Sanchez, W. Schulmeyer, H. Traxler, A. Ureña, J.G. Van Der Laan, L. Veleva, S. Wahlberg, M. Walter, T. Weber, T. Weitkamp, S. Wurster, M.A. Yar,

J.H. You, A. Zivelonghi, Recent progress in research on tungsten materials for nuclear fusion applications in Europe, J. Nucl. Mater. 432 (2013) 482–500, https://doi.org/10.1016/j.jnucmat.2012.08.018.
[8] X.Y. Ding, L.M. Luo, H.Y. Chen, G.N. Luo, X.Y. Zhu, X. Zan, J.G. Cheng, Y.C. Wu, Fabrication of W-1 wt.% TiC composites by spark plasma sintering, Fusion Eng. Des. 92 (2015) 29–34, https://doi.org/10.1016/j.fusengdes.2015.01.003.
[9] L. Veleva, R. Schaeublin, M. Battabyal, T. Plociski, N. Baluc, Investigation of microstructure and mechanical properties of W-Y and W-Y2O3materials fabricated by powder metallurgy method, Int. J. Refract. Met. Hard Mater. 50 (2015) 210–216, https://doi.org/10.1016/j.ijrmhm.2015.01.011.
[10] R. Liu, Y. Zhou, T. Hao, T. Zhang, X.P. Wang, C.S. Liu, Q.F. Fang, Microwave synthesis and properties of fine-grained oxides dispersion strengthened tungsten, J. Nucl. Mater. 424 (2012) 171–175, https://doi.org/10.1016/j.jnucmat.2012.03.008.
[11] Z. Dong, N. Liu, Z. Ma, C. Liu, Q. Guo, Y. Liu, Preparation of ultra-fine grain W-Y2O3 alloy by an improved wet chemical method and two-step spark plasma sintering, J. Alloys Compd. 695 (2017) 2969–2973, https://doi.org/10.1016/j.jallcom.2016.11.364.
[12] M.A. Yar, S. Wahlberg, H. Bergqvist, H.G. Salem, M. Johnsson, M. Muhammed, Chemically produced nanostructured ODS-lanthanum oxide-tungsten composites sintered by spark plasma, J. Nucl. Mater. 408 (2011) 129–135, https://doi.org/10.1016/j.jnucmat.2010.10.060.
[13] I. Wesemann, W. Spielmann, P. Heel, A. Hoffmann, Fracture strength and microstructure of ODS tungsten alloys, Int. J. Refract. Met. Hard Mater. 28 (2010) 687–691, https://doi.org/10.1016/j.ijrmhm.2010.05.009.
[14] P. Norajitra, L.V. Boccaccini, E. Diegele, V. Filatov, A. Gervash, R. Giniyatulin, S. Gordeev, V. Heinzel, G. Janeschitz, J. Konys, W. Krauss, R. Kruessmann, S. Malang, I. Mazul, A. Moeslang, C. Petersen, G. Reimann, M. Rieth, G. Rizzi, M. Rumyantsev, R. Ruprecht, V. Slobodtchouk, Development of a helium-cooled divertor concept: Design-related requirements on materials and fabrication technology, J. Nucl. Mater. 329–333 (2004) 1594–1598, https://doi.org/10.1016/j.jnucmat.2004.04.137.
[15] S. Wurster, N. Baluc, M. Battabyal, T. Crosby, J. Du, C. García-Rosales, A. Hasegawa, A. Hoffmann, A. Kimura, H. Kurishita, R.J. Kurtz, H. Li, S. Noh, J. Reiser, J. Riesch, M. Rieth, W. Setyawan, M. Walter, J.H. You, R. Pippan, Recent progress in R&D on tungsten alloys for divertor structural and plasma facing materials, J. Nucl. Mater. 442 (2013) 181–189, https://doi.org/10.1016/j.jnucmat.2013.02.074.
[16] M. Mabuchi, K. Okamoto, N. Saito, T. Asahina, T. Igarashi, Deformation behavior and strengthening mechanisms at intermediate temperatures in W-La2O3, Mater. Sci. Eng. A. 237 (1997) 241–249, https://doi.org/10.1016/S0921-5093(97)00420-6.
[17] M. Rieth, R. Doerner, A. Hasegawa, Y. Ueda, M. Wirtz, Behavior of tungsten under irradiation and plasma interaction, J. Nucl. Mater. 519 (2019) 334–368, https://doi.org/10.1016/j.jnucmat.2019.03.035.
[18] C. Linsmeier, M. Rieth, J. Aktaa, T. Chikada, A. Hoffmann, J. Hoffmann, A. Houben, H. Kurishita, X. Jin, M. Li, A. Litnovsky, S. Matsuo, A. Von Müller, V. Nikolic, T. Palacios, R. Pippan, D. Qu, J. Reiser, J. Riesch, T. Shikama, R. Stieglitz, T. Weber, S. Wurster, J.H. You, Z. Zhou, Development of advanced high heat flux and plasma-facing materials, Nucl. Fusion. 57 (2017), https://doi.org/10.1088/1741-4326/aa6f71.
[19] S. Antusch, L. Commin, M. Mueller, V. Piotter, T. Weingaertner, Two component tungsten powder injection molding - An effective mass production process, J. Nucl. Mater. 447 (2014) 314–317, https://doi.org/10.1016/j.jnucmat.2013.11.007.
[20] T. Loewenhoff, S. Antusch, G. Pintsuk, M. Rieth, M. Wirtz, High pulse number thermal shock testing of tungsten alloys produced by powder injection molding, Nucl. Mater. Energy. 20 (2019) 100680, , https://doi.org/10.1016/j.nme.2019.100680.
[21] Y. Li, T.W. Morgan, J.A.W. van Dommelen, S. Antusch, M. Rieth, J.P.M. Hoefnagels, D. Terentyev, G. De Temmerman, K. Verbeken, M.G.D. Geers, Fracture behavior of tungsten-based composites exposed to steady-state/transient hydrogen plasma, Nucl. Fusion. (2020), https://doi.org/10.1088/1741-4326/ab77e7.
[22] S. Antusch, L. Commin, J. Heneka, V. Piotter, K. Plewa, H. Walter, A new fully automatic PIM tool to replicate two component tungsten DEMO divertor parts, Fusion Eng. Des. 88 (2013) 2461–2465, https://doi.org/10.1016/j.fusengdes.2013.04.037.
[23] S. Antusch, D.E.J. Armstrong, T. Ben Britton, L. Commin, J.S.K.L. Gibson, H. Greuner, J. Hoffmann, W. Knabl, G. Pintsuk, M. Rieth, S.G. Roberts, T. Weingaertner, Mechanical and microstructural investigations of tungsten and doped tungsten materials produced via powder injection molding, Nucl. Mater. Energy. 3–4 (2015) 22–31, https://doi.org/10.1016/j.nme.2015.04.002.
[24] A. Giannattasio, Z. Yao, E. Tarleton, S.G. Roberts, Brittle-ductile transitions in polycrystalline tungsten, Philos. Mag. 90 (2010) 3947–3959, https://doi.org/10.1080/14786435.2010.502145.
[25] R.G. Abernethy, J.S.K.L. Gibson, A. Giannattasio, J.D. Murphy, O. Wouters, S. Bradnam, L.W. Packer, M.R. Gilbert, M. Klimenkov, M. Rieth, H.C. Schneider, C.D. Hardie, S.G. Roberts, D.E.J. Armstrong, Effects of neutron irradiation on the brittle to ductile transition in single crystal tungsten, J. Nucl. Mater. 527 (2019), https://doi.org/10.1016/j.jnucmat.2019.151799.
[26] C. Yin, D. Terentyev, T. Pardoen, A. Bakaeva, R. Petrov, S. Antusch, M. Rieth, M. Vilémová, J. Matějíček, T. Zhang, Tensile properties of baseline and advanced tungsten grades for fusion applications, Int. J. Refract. Met. Hard Mater. 75 (2018) 153–162, https://doi.org/10.1016/j.ijrmhm.2018.04.003.
[27] P. Jia, L. Chen, J. Rao, Y. Wang, Q. Meng, Y. Zhou, Evolution of Phase, Microstructure and ZrC Lattice Parameter in Solid-solution-treated W-ZrC Composite, Sci. Rep. (2017), https://doi.org/10.1038/s41598-017-06301-0.
[28] J.H. Kim, C. Park, J. Lim, S. Kang, Microstructures and properties of ultrafine grained W-ZrC composites, J. Alloys Compd. 623 (2015) 282–289, https://doi.org/10.1016/j.jallcom.2014.10.128.
[29] G.M. Song, Y. Zhou, Y.J. Wang, The microstructure and elevated temperature strength of tungsten-titanium carbide composite, J. Mater. Sci. 37 (2002) 3541–3548, https://doi.org/10.1023/A:1016583611632.
[30] H. Holleck, Binäre und Ternäre Cabide und Nitride der Übergangsmetalle und ihre Phasenbeziehungen, Binäre Und Ternäre Cabide, Und Nitride Der Übergangsmetalle Und Ihre Phasenbeziehungen. 340 (1981).
[31] R. Seshadri, R. Basu, Periodic table of the elements, (n.d.). https://www.mrl.ucsb.edu/~seshadri/Periodic/index.html (accessed February 19, 2020).
[32] U. of Cambridge, The interactive Ellingham Diagram, (n.d.). https://www.doitpoms.ac.uk/tlplib/ellingham_diagrams/interactive.php (accessed February 25, 2020).
[33] E. Lassner, W.-D. Schubert, Tungsten: properties, chemistry, technology of the element, alloys, and chemical compounds, Springer Science & Business media, LLC, New York, 1999.
[34] H.J. Borchardt, Yttrium-Tungsten Oxides, Inorg. Chem. 2 (1963) 170–173, https://doi.org/10.1021/ic50005a043.
[35] A.J. Craven, L.A.J. Garvie, Electron Energy Loss Near Edge Structure (ELNES) on the Carbon K-Edge in Transition Metal Carbides with the Rock Salt Structure, Microsc. Microanal. Microstruct. (1995), https://doi.org/10.1051/mmm:1995109.
[36] J. Zhang, F. Paumier, T. Höche, F. Heyroth, F. Syrowatka, R.J. Gaboriaud, H.S. Leipner, Electron energy-loss spectroscopy investigation of Y2O3 films on Si (001) substrate, Thin Solid Films. 496 (2006) 266–272, https://doi.org/10.1016/j.tsf.2005.08.337.
[37] F. de la Peña, E. Prestat, V.T. Fauske, P. Burdet, P. Jokubauskas, M. Nord, T. Ostasevicius, K.E. MacArthur, M. Sarahan, D.N. Johnstone, J. Taillon, J. Lähnemann, V. Migunov, A. Eljarrat, J. Caron, T. Aarholt, S. Mazzucco, M. Walls, T. Slater, F. Winkler, Pquinn-dls, B. Martineau, G. Donval, R. McLeod, E.R. Hoglund, I. Alxneit, D. Lundeby, T. Henninen, L.F. Zagonel, A. Garmannslund, hyperspy/hyperspy: HyperSpy v1.5.2, (2019). https://doi.org/10.5281/zenodo.3396791.